# Universality in early-stage growth of phase-separating domains near the critical point

Ana Oprisan, Sorinel Adrian Oprisan, John Hegseth, Yves Garrabos, Carole Lecoutre-Chabot, Daniel Beysens

# Universality in early-stage growth of phase-separating domains near the critical point

Ana Oprisan and Sorinel A. Oprisan
*Department of Physics and Astronomy, College of Charleston, 60 George Street, Charleston, South Carolina 29424, USA*

John J. Hegseth
*Department of Physics, University of New Orleans, 2000 Lakeshore Drive, New Orleans, Louisiana 70148, USA*

Yves Garrabos, Carole Lecoutre-Chabot, and Daniel Beysens
*Institut de Chimie de la Matiere Condensee de Bordeaux, University de Bordeax I, Avenue de Dr. Schweitzer, F 33608 Pessac Cedex, France*

(Received 9 February 2008; published 19 May 2008)

We present both the experimental and computational methods and results of phase-separating experiments performed with sulfur hexafluoride ($SF_6$) close to its critical density. These experiments were performed in microgravity to suppress buoyancy and convection-driven effects. Phase separation under reduced gravity is analyzed for both 0.3 mK and 3.6 mK temperature quenches in order to derive the early-stage growth law. We found a 1/3 growth law for early stages of phase separation for a volume fraction of minority domains of 50%. Our findings support the hypothesis of a crossover between Brownian motion and hydrodynamic effects in the early stages of phase separation. The temperature inside the bulk of the pure fluid was estimated using a proposed histogram method. Our histogram method allowed temperature estimation below thermistors' sensitivity and detected small temperature variations inside the bulk of the pure fluid.

DOI: 10.1103/PhysRevE.77.051118 PACS number(s): 64.60.F−, 68.35.Rh, 81.10.Mx, 81.70.Ha

## I. INTRODUCTION

According to the laws of thermodynamics, a system will evolve toward a minimum of its free energy. It is often convenient to measure the distance from a target steady state by means of order parameters and express the free energy as an analytical function in respect to the appropriately chosen order parameters [1]. If the free energy has two minima, then there are two phases that coexist and two equilibrium values of the order parameter. The process that occurs when a system undergoes a change of its free energy shape from one minimum to two minima is called phase separation. When a state variable, such as temperature, changes and initiates phase separation, the resulting behavior is a dynamic out-of-equilibrium growth of minority domains. Phase separation became a natural testing ground for nonequilibrium statistical physics and it is also a problem of considerable practical importance. Engineering applications are especially important in two-phase heat and mass transfer processes. Phase separation is also ubiquitous in materials processing, e.g., metallic alloys [2], polymer alloys, and polymer-liquid crystal mixtures [3]. The late-stage growth of the minority domains is important in materials processing because the final properties of the material depend greatly on the final morphology when phase separation is completed [2]. To help understand the domain growth process, an important step is to find natural scales to measure observable quantities. Previous results in phase-separation experiments have shown that near-critical fluids have such a natural length and time scale [4]. Two types of morphologies and growth kinetics have consistently been observed: (1) Slow growth with disconnected domains, and (2) fast growth with connected domains. These results have suggested that phase-separation phenomenon exhibits universality, i.e., the growth laws may be described by master curves that are valid for all fluids within these two scale factors. Recent results obtained using colloid-polymer mixture in microgravity showed a clear crossover from early-stage to late-stage spinodal decomposition for large quenches [5]. In this paper, we present experimental results, derive the early-stage growth curves, and discuss the temperature derivation based on our histogram method.

## II. BACKGROUND

### A. Pure fluids and binary mixtures

Binary liquids near the critical point of miscibility belong to the same universality class as pure liquids (cf. the three-dimensional Ising model [2,6]). Their dynamic behavior, however, can be marked differently, especially in a gravitational field [7]. This difference can be seen from the order parameter $M$ ($M$ is a generic variable that describes or controls a phase transition). $M$ is the concentration difference $M=c-c_c$ for liquid mixtures, where $c$ is the concentration and $c_c$ is the critical concentration. At $c_c$, the osmotic compressibility diverges and the mutual diffusion coefficient goes to zero. When $T$ is changed to induce phase separation, sedimentation usually occurs because one phase is denser than the other. An appropriate order parameter ($M$) for pure fluids is the dimensionless density difference $M=(\rho-\rho_c)/\rho_c$, where $\rho$ is the density and $\rho_c$ is the critical density. At the critical point, the isothermal compressibility ($k_T$) diverges and the thermal diffusivity vanishes. Because pure fluids near the critical temperature have a very large isothermal compressibility, they are very sensitive to the Earth's gravitational field [8]. Experiments are complicated by the very high compressibility of the fluid that induces density gradients even in the single-phase regime. Convective flows, often turbulent, are also observed [9]. These properties lead to a

 

very fast heat transport mechanism, the so-called piston effect [10,11]. Specifically, the small diffusivity localizes the heat taken by the fluid to a boundary layer near the boundary between the external heat source and the fluid. At the same time, a large expansion coefficient decreases the density in this boundary layer so that the bulk of the fluid senses the temperature decrease very rapidly, which resembles the effect produced by a real piston. The piston effect allows thermal equilibration in the bulk of a fluid sample to be limited only by the thermal response of the thermostat [12–14]. This fast thermalization occurs at the expense of a changed density in the boundary layer, so that the bulk density decreases. This unavoidable lack of homogeneity between the boundary layer and the bulk fluid modifies the separation process. The boundary layer has a negligible effect on nucleation and phase separation in the bulk. However, the wetting film can only be seen when the growing droplets are of the order of the cell thickness and a large-scale bubble begins to form.

During an actual phase-separation experiment, pure fluids and binary liquids are always sensitive to convection and/or sedimentation. Because such externally imposed convective flows tend to increase the growth rates of minority phase domains, attempts have been made to avoid buoyancy driven convection in terrestrial experiments by preparing density-matched liquid mixtures, e.g., by adding a small amount of deuterated cyclohexane in a cyclohexane-methanol mixture (CM). These attempts show that it is practically impossible to avoid long-term sedimentation in terrestrial experiments because density matching can never be perfect. Although liquid mixtures and pure fluids are formally part of the same universality class, there are significant differences also, starting with the order parameter itself. These differences are especially large when comparing transport and interfacial properties in the phase separated regime. The corresponding diffusion coefficients, $D_m$ for liquid mixtures and $D_{\mathrm{th}}$ for pure fluids, both disappear at the critical point and create critical slowing down. During the phase-separation process, in the absence of convection, mass transport processes are purely diffusive in a liquid mixture, while in pure fluids the transport of heat and mass are strongly coupled by the latent heat of vaporization. The viscosity, $\eta$, can also be quite different. This will lead to large differences in the fluctuation relaxation time $\tau$. $\eta$ for $SF_6$, for example, is 30 times larger than $\eta$ for the CM mixture.

### B. Nucleation and generalized nucleation

The classical view of phase separation is that of metastable nucleation and spinodal decomposition [14–18]. According to this approach, the single-phase state may be maintained in a metastable state because the free energy costs associated with the two-phase interface produce a local free energy minimum in the single-phase state. If a fluctuation is large enough to overcome the energy barrier associated with the interfacial energy, then it will nucleate a new phase and droplets will grow. Nucleation centers of some sort are required for droplet growth when in the metastable state. In spinodal decomposition region, there is no local minimum in the mean-field free energy so that the one-phase state is unstable and the two phases appear spontaneously. Under the usual conditions of phase separation, unstable and metastable potentials may be clearly defined using the mean-field approximation [8]. This approximation assumes a very small level of fluctuations, so that nucleation of a growing domain is more likely to occur on a foreign particle, such as raindrops forming on dust particles, or on a container wall. Near the critical point, the fluctuations are large and the mean-field approximation breaks down. As a result another form of generalized nucleation takes place [19]. The presence of large fluctuations around the mean and the small interfacial energy barrier, a property of near-critical fluids that is constantly penetrated, suggests that each fluctuation is a potential nucleation site. During generalized nucleation, droplets form uniformly inside the fluid, much as in the spinodal decomposition case. Other experimental results in liquid mixture previously described the crossover from nucleation to spinodal decomposition [20].

### C. Influence of hydrodynamics and Brownian motion

Phase separation has been of great theoretical interest over the last several decades. The work by Siggia has initiated many attempts to explain the two growth laws by considering hydrodynamic arguments [21]. Several groups have done large-scale direct numerical simulations by using different approaches to solve coupled equations involving diffusion and hydrodynamics [14,22–26]. Some of these simulations have recovered a linear growth law at late stages [21,25]. Some other simulations were unable to reach the late stages of separation but did calculate the transient values of the growth exponent, which was found to be between 1 and 1/3. More recently, some fully three-dimensional simulations of phase-separating fluid have found the transition from slow growth to fast growth. This transition appears to be controlled by the interparticle distance or the volume fraction [27,28]. The above-mentioned numerical simulations confirm the predictions made earlier in [29]. The explanation of the existence of the two different regimes, their relation to the pattern morphology, and the absence of a crossover was explained by considering coalescence as the main mechanism for growth in all cases so that the transition corresponds to the onset of hydrodynamics effects that start at a particular volume fraction. In addition, the linear growth law was found by considering the hydrodynamic effects of coalescence when many droplets are close together. At high equilibrium volume fraction ($\phi$) droplet coalescence is a leading candidate for the underlying growth mechanism at late times in both the "fast" and the "slow" growth case. In the "slow" growth case, the Brownian motion of the droplets implies a characteristic collision rate of the droplets. When randomly moving spherical droplets collide, they coalesce and grow [30,31]. This growth mechanism also leads to a $t^{1/3}$ growth law [19]. The "fast" growth at late times is also explained using a coalescence mechanism [21,32]. At higher values of volume fraction ($\phi$), droplets also form as a result of coalescence of two neighboring droplets. However, two coalescing droplets induce coalescence with another nearby droplet through hydrodynamic lubrication interactions. Although in

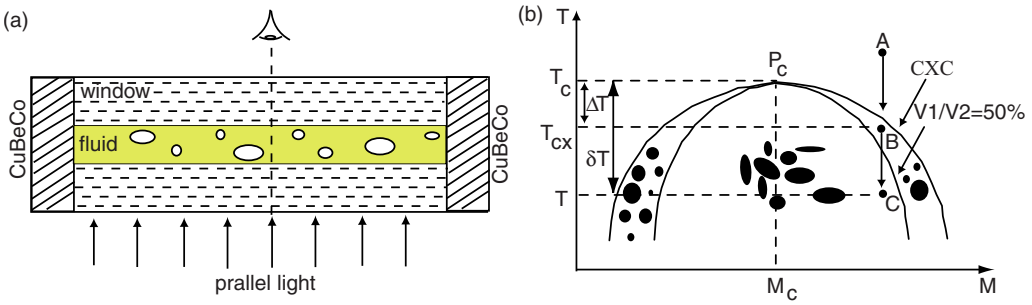


FIG. 1. (Color online) Cross section of the cylindrical sample cell (a). The fluid volume is contained between two sapphire windows and a CuBeCo alloy ring. The cell consists of a $D=12$ mm diameter cylinder made of CuBeCo containing a thin layer, 9 mm thick of $SF_6$, sandwiched between two sapphire windows. Growth and morphology phase diagram of $SF_6$ (b). The supercritical fluid at initial temperature $T_i$ (point $A$), with an off-critical density $\delta M$ is quenched below the coexistence curve (CXC) and droplets of vapor (volume $V1$) and liquid (volume $V2$) nucleate and grow. Previous experiments show that the curve $V1/V2 \sim 50\%$ separates a region of slow growth ($A$-$B$, quench 50 mK below CXC) where the droplets are disconnected and grow as $t^{1/3}$, and a region of fast growth ($A$-$C$, quench 3 mK below CXC), where the droplets are interconnected and grow linearly in $t^1$. By adjusting the piston between quenches, different final points, could be reached [see points $D$, $E$, and $F$ in panel (b)]. The critical point, $Pc$, is characterized by critical temperature $Tc=45.54$ °C, and the $Mc$ corresponding to the critical density $\rho_c=0.737$ g/cm$^3$.

principle such an interaction should be repulsive, in the presence of a "mean field" of many neighboring droplets that also interact repulsively induces a positive feedback that reinforces droplets' coalescence. The characteristic time between coalescence events is controlled by the hydrodynamic process. The hydrodynamic mechanism can only work when the droplets are closely packed, i.e., for large volume fraction $\phi$. In addition, the hydrodynamic interactions can generate chain reactions of successive coalescences that create interconnected patterns. It was also shown that at a "critical" value of the volume fraction the hydrodynamic mechanism will dominate over the Brownian mechanism and the transition from "slow" to "fast" growth occurs. The hydrodynamic model also predicted a sharp transition between "fast" growth and "slow" growth regimes at $\phi \approx 0.3$ [29]. The above cited theoretical studies underline the importance of droplet interaction for the growth and morphology of minority domains. When the droplets are far apart, growth is slow and follows a $t^{1/3}$ growth law for late times through a diffusion process of either coalescence by Brownian motion or by diffusion of mass (the Lifshitz-Slyozov mechanism). When the growing domains are close together, they interact through hydrodynamics and grow quickly. There appears to be several growth laws in the latter case depending on the type of interaction of flow that is present. If the interactions are assumed to be in the limit of large viscosity or small Reynolds number the growth law is $t^1$. In the limit of large Reynolds number, where inertial effects dominate, other growth laws have been predicted. Furukawa [9,33] predicted growth exponents between 2/5 and 2/3 depending on the temperature quench depth. All numerical experiments assumed that the boundary layers are of negligible importance and it is difficult to see how such an assumption can be realized in a system of closely spaced droplets where interfacial boundaries are clearly a dominant feature. Despite multiple explanations and diverging approaches, one trend was clearly suggested both in experimental and theoretical studies [9]: The exponent of growth law increases when external flows are applied to the system. This has been clearly observed in a phase-separation experiment with a slight temperature gradient [34]. In that experiment the thermal capillary flow clearly increases the exponent of the growth law. The roles of hydrodynamic instabilities, such as Rayleigh-Taylor [35] and Maragoni instability [36], in pure fluids or solute-capillary flows in binary liquids have not been considered in all possible detail. In addition, most of the previous studies have considered linear approximations to the fully nonlinear hydrodynamic equations. In this paper, we present results regarding phase separation in pure fluid, in the early stage of the fast growth regime.

## III. EXPERIMENT

To prevent external flows and sedimentation from influencing the growth processes, these experiments were performed in a microgravity environment using the Alice-II instruments [37]. This instrument is specially designed to obtain high precision temperature control with stability of approximately 10 $\mu$K over 50 h, and repeatability of approximately 40 $\mu$K over 7 days. To place the samples near the critical point, constant mass cells were prepared with a high precision density, to 0.02%, by observing the volume fraction change of the cells as a function of temperature on the ground [38]. Two cylindrical sapphire windows 12 mm diameter and 9.0 mm long are pressed into a copper block with a corresponding cylindrical hole and glued to the copper at the sides of the sapphire. This method avoids the unknown volume associated with $o$-rings, allowing the above high precision density measurements to be verified. A layer of $SF_6$, was sandwiched between the two sapphire windows and surrounded by a copper housing in the optical cell shown in Fig. 1. Temperature control and precise quenches are provided by thermoelectric (Peltier) heat pumps. The temperature is quenched below the coexistence temperature $T_{cx}$, as shown in Fig. 2, while the liquid-gas interface was visualized through light transmission normal to the windows.

### A. Cells and quenches

The sample cell [Fig. 1(a)] includes three thermistors (Th1, Th2, and Th3) used to measure the temperature inside

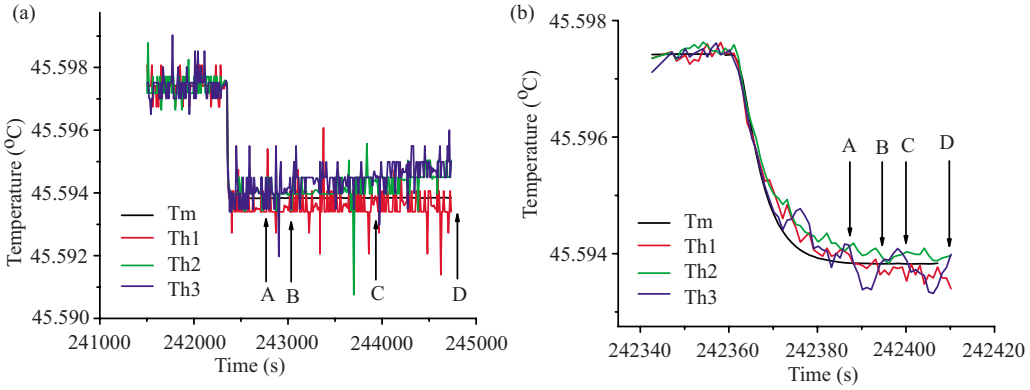


FIG. 2. (Color online) Temperature quench of 3.6 mK measured by three thermistors (Th1, Th2, and Th3) placed inside the SCU and one mounted on the external wall ($T_m$) of the cell. The experiment spanned over 1 hour (a), but the temperature settled after about 1 minute (b). The vertical arrows point to specific time markers and relate to images in Fig. 3 and Fig. 5.

the fluid with a response time of approximately 10 ms. A sealed piston to the left-hand side can slide in and out of the cell volume to change the fluid's average density at a constant mass. The volume of the cell was initially adjusted to $M=0.02\%$ on the ground so that the second run was performed at the critical density. In order to allow this piston to operate, we used a cell that is thicker than usual ($L=4.340$ mm), for an aspect ratio of $\Gamma=D/L=2.765$. The thick cell allowed the bubbles to grow to a larger size before wetting effects from the wall influenced the growth. It also prevents the thermal boundary layer at the sapphire windows or copper sidewalls from influencing the *in-situ* thermistors. The gas droplets in the full field of the cell were visualized through light transmission normal to the windows using a LED light source at 633 nm. Optical microscopy of 3.1 $\mu$m resolution was used to visualize density fluctuations and small droplets. The volume fraction of the gas phase is a key parameter for these experiments. Adjusting the temperature quench depth controlled this parameter. This is possible because of the lever rule that relates the volume fraction of the gas to the temperature quench $\delta T$,

$$\phi = \frac{M^+ - M}{M^+ - M} = \frac{1}{2}\left[1 - \left(1 + \frac{\Delta T}{\delta T}\right)^{-\beta}\right], \tag{1}$$

where $M=\delta\rho/\rho_c$ is the order parameter ($\delta\rho=\rho-\rho_c$), $\delta T=|T_c-T|$ is the quench depth with respect to the critical temperature, $\Delta T=|T_c-T_{cx}|$ is the quench depth between the coexistence temperature ($T_{cx}$) and critical temperature ($T_c$), and $\beta=0.325$ is a universal exponent.

The coexistence curve [Fig. 1(b)] near the critical point is given by $M=\pm B(1-T/T_c)^{\beta}$, where $B$ is a system-dependent parameter ($B=1.6$ for $SF_6$). The coexistence temperature is different for each density and must be accurately determined at each density in order to estimate $\Delta T$ accurately. The quenches of the phase-separation experiments concurrently find $T_{cx}$. Alice-II initially finds $T_{cx}$ by quenching through the temperature range corresponding to $T_{cx}$ several times while measuring the turbidity. Near the critical point, the turbidity becomes very large due to critical opalescence. The turbidity is quantified by measuring the light transmission signal of a laser beam that traverses the fluid. The intensity of the laser beam is measured with photodiodes before and after it enters the fluid sample. Before each pass through $T_{cx}$, the cell was heated to 1 K above $T_c$ where it equilibrates to a homogenous state. Initially nine 0.10 K temperature quenches were delivered through the $\pm 0.50$ K region around $T_{cx}$ and the turbidity was measured at each temperature. The range of largest turbidity around $T_{cx}$ is then probed with nine additional 0.050 K quenches through the $\pm 0.250$ K regions around $T_{cx}$ followed by a single 25 mK and a 15 mK quench to reduce the uncertainty range of $T_{cx}$. The last 15 mK temperature quench region is then quenched through in 1 mK steps and $T_{cx}$ is measured with $\pm 0.5$ mK error. Because of the heating effect of the laser beam this initial search is only precise to within 1 mK. One unintended consequence of using a thicker cell ($L=4.340$ mm) was that the search procedure overestimated $T_{cx}$ because this increased thickness decreased the light intensity and made the cell appear more turbid at a higher temperature than expected from previous experiments. As a result, many of the automated quenching sequences missed phase separations altogether and some that did separate were too turbid to visualize the droplets and to find a quantitative growth law.

Each of the phase-separation runs consisted of three sets of quenches. First, a large temperature quench was performed through the expected $T_{cx}$ estimated during the $T_{cx}$ search protocol. This temperature quench resulted in uniform separation and reliable growth data for each run. In the two-phase-separation runs reported in detail here, the first quench in run 1 was of 2.3 mK, placing the system 0.70 mK below $T_{cx}$. The first quench in the second run was of 3.6 mK that placed the system 0.36 mK below $T_{cx}$ [Fig. 1(b)]. The second set of quenches consisted of a series of 0.3 mK quenches that stepped through the same range as the large quench. The third and final set of thermal quenches consisted of 0.1 mK quenches, which were the limit of Alice-II's quenching ability that also stepped through the expected $T_{cx}$. After each thermal quench the fluid visualization attempted to detect if phase separation occurred. If no phase separation occurred, then the temperature was above $T_{cx}$; otherwise, the growth of the droplets was recorded using a CCD camera and digital recording tape. The system was uniformly illuminated and recordings were made of both the full view and the micro-

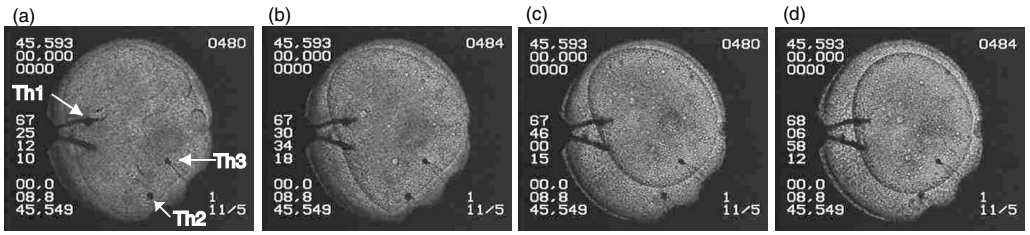


FIG. 3. Temporal and morphological evolution related to 3.6 mK temperature quench corresponding to temporal markers indicated by vertical arrows in Fig. 2(a). The three thermistors measure the temperature inside the SCU (see Fig. 2). Out of the three groups of numbers marked on the left-hand side of each image, the central group shows the recording time in hours, minutes, seconds, and fractions of seconds. Toward the end of the recorded sequence (d) only the third thermistor is left inside the gas bubble and overheats [Fig. 2(a)].

scopic field of the cell. This microscopic field was a square of 0.9 mm in width. By visualizing the phase separation in uniform illumination the effect of light heating was minimized and $T_{cx}$ was estimated to a higher precision.

The small temperature quenches produce inhomogeneous separations and are usually only used to determine $T_{cx}$ to higher precision. We did, however, analyze the separation from the 0.3 mK quench in the second run. Because the system separated on the very last 0.3 mK quench, $T_{cx}$ was very near the bottom of the 3.6 mK range of the first large quench. Unfortunately, in an attempt to economize on time, the 0.1 mK quenches of the third sequence stopped at about 1 mK above $T_{cx}$. We were, however, able to visualize density fluctuations using microscopy and analyze the microscope images in these 0.3 mK quenches in order to estimate $T_{cx}$ as discussed below [39].

### B. The 3.6 mK quench

The temperature inside the sample cell unit (SCU) initially follows the temperature ($T_m$) measured by the thermistor placed on the external wall of the SCU. However, the temperature inside the SCU, does not follow the $T_m$ at the bottom of the quench, but seems to relax more slowly to the final temperature. Unfortunately, the internal temperature is only known within 1 mK precision of the thermistors used. The decrease in $T_m$, shown in Fig. 2(b), marked the beginning of the cooling pulse to the SCU and the temperature decrease in Th1, Th2, and Th3 is immediate while $T_m$ lags. This verifies that the proper origin of time is the time of the heat pulse recorded by $T_m$. Figure 2(b) shows that the time lag of $T_m$ is almost 10 s.

An interesting feature of this 3.6 mK quenching experiment was an upward drift of temperature measured inside the SCU at later times [Fig. 2(a)]. This upward drift corresponds to the formation of the large bubble (Fig. 3). In Fig. 3(a) the bubble is not yet well defined and the three thermistors, Th1, Th2, and Th3 are all at approximately the same temperature. In Fig. 2(a), Th2 and Th3 begin to drift upward. This upward drift correlates with the increased contrast of the interface of the large bubble and the presence of thermistors Th2 and Th3 in the interior of the large bubble while Th1 remained outside. In Figs. 3(c) and 3(d) Th1 stayed outside of the interface and remained at the same temperature as $T_m$. Th3 remained in the bubble and its temperature continued to drift upward by 1 mK over approximately 30 min. Th2's temperature also drifts upward, but this thermistor was clearly outside of the bubble. The largest temperature drift of Th2 occurred near the boundary of the bubble [Fig. 3(d)].

### C. The 0.3 mK quench

Although the 0.3 mK temperature quench did not result in homogenous separation, the microscopic observations did provide a good visualization of the nucleation process in near-critical fluids. In the case of the 0.3 mK temperature quench experiment, the images were divided in two groups: The "up" group, with one representative example shown in (see Fig. 4) Fig. 5(a), and the "down" group, with representative images of SCU shown in Figs. 5(b) and 5(c). The video recording for the 0.3 mK temperature quench experiment started when the fluid was very turbid due to critical opalescence. The spatial size of fluctuations grew on the last part of the "down" plateau and eventually the fluid separates into gas and liquid phases [Fig. 5(d)].

## IV. EXPERIMENTAL RESULTS AND DISCUSSION

Image processing tools such as filtering and fast Fourier transforms (FFT) were used to extract information and phase separation from the recorded images corresponding both to 0.3 mK and 3.6 mK quenches. The video recording of the "down" region shows intensity fluctuations over a very small

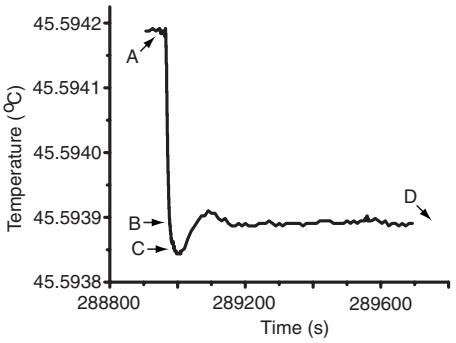


FIG. 4. The last 0.3 mK temperature quench steps through the critical temperature. The temperature is measured by the thermistor $T_m$. The two distinctive regions of the quench were called "up" (before quench) and "down" (after quench). Time markers indicated by arrows and labeled *A*, *B*, *C*, and *D*, correspond to images shown in Fig. 5.

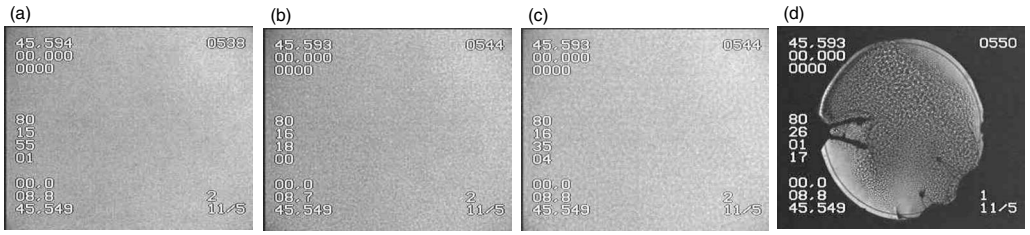


FIG. 5. Microscopic and full views of SCU during the 0.3 mK quench for "up" (a) and "down" [(b) and (c)] regions. The last image shows the phase-separating domains (d) that occurs toward the final stage of "down" plateau. The image sequence corresponds to time markers shown in Fig. 4.

spatial distance, close to the resolution of the movie. At the same time, the optical noise is also short range and overlaps with the intensity fluctuations determined by actual density fluctuations taking place inside the fluid. Therefore, subtracting a background image is not very effective in reducing optical noise for the "down" region [40]. As a result, the first step in image processing of the "down" region was to use $n$-point filter to reduce the effect of optical noise. Different moving average filter sizes were used to test their influence on the FFT power spectrum. For the purpose of noise reduction, a filter the size of nine pixels proved to give the clearest contour of the color-coded FFT power spectrum [39]. The peak value of the wave number ($k_m$) of the radial average of the power spectrum varies with the size of the averaging filter (not shown). A plot of $k_m$ versus the filter's size revealed the existence of two distinct regions: Smoothing without cutting short range fluctuations, and severe filtering revealing only large scale fluctuations (data not shown). For relative small values of the filter's size (less than 10 units), the wave number is relatively high and quickly decreasing with the increase of the filter's size. This suggests that, although the filter is still effective in smoothing the images, it also allows the small range fluctuations (high wave-number values) to pass. On the other end, a filter size around 10 units filtered most of the short-scale fluctuations, including optical noise, and is still capturing fluctuations over an intermediate range.

### A. Analysis of images recorded during the "down" region of the 0.3 mK quench

The following procedure was used to extract information from recorded images. We first applied a $n$-point filter to a recorded image in the "down" region to obtain the corresponding filtered image. The latest was subtracted from the original image and the resulting image was called fluctuation image [Fig. 6(a)].

We used the above procedure to eliminate the background noise for recorded frames in the 0.3 mK quench and 3.6 mK quench. Two-dimensional FFT and their corresponding power spectra for the fluctuation images such as those shown in Fig. 6(b) were performed to estimate the average wave number $k_m$. The dark ring in the power spectra corresponds to randomly oriented structures. This distinctive structure of significantly high amplitude is an indication of large-scale fluctuations. Based on the radial symmetry of the power spectra [Fig. 6(b)], we averaged the power spectra along all radii centered on the dc component. The broad peak in the plot of the radial average of the power spectrum (Fig. 7) corresponds to the ring in the power spectrum shown in Fig. 6(b). The average power spectrum revealed a characteristic wavelength that emerged from the fluctuations at a given time.

The maximum of the broad peak of the radial average of the power spectrum is related to the characteristic length of the fluctuations [41]. The relationship between the spatial and frequency domains is [42],

$$k = \frac{k_m}{N\Delta x}, \tag{2}$$

where $N=172$ is the total number of pixels in the image, $\Delta x=3.1$ $\mu$m represents the image resolution in spatial domain, and $k_m$ represents the dimensionless value of the maximum of the broad peak in the radial average power spectrum shown in Fig. 7. The value for the wave vector is related to the characteristic length of the correlated fluctuations ($\lambda$) as follows [43]:

$$k = 2\pi/\lambda. \tag{3}$$

For example, a value of $k_m=29$ arbitrary units corresponds with a characteristic length of 7.45 $\mu$m. The thermistors sensitivity is below the temperature quench depth and the only way to determine the temperature for each image is to use image analysis techniques. The method we developed to determine the temperature is based on the characteristics of the histograms and does not take into consideration the spatial position of a pixel in the recorded image.

The histograms of the fluctuation images [see Fig. 6(a)] are shown in Fig. 8. The histograms have a Gaussian shape [43] and are in good agreement with the statistic of fluctuations. The histogram has a width $\sigma_i$ that relates to the variance of gray level intensity, $\langle \delta i^2 \rangle$, in the recorded image. First we considered that the intensity of the scattered light is proportional to the variation in the density of the fluid

$$\langle \delta I^2 \rangle = c^2 \langle \delta \rho^2 \rangle, \tag{4}$$

where $\delta I = \langle I - I_0 \rangle / I_0$, $c$ is a dimensionless temperature-dependent coefficient. The local density fluctuations, $\langle \delta \rho^2 \rangle = \langle \Delta \rho^2 \rangle / \rho_c^2$, can be determined by measuring the fluctuations of the intensity of scattered light, $\langle \delta I^2 \rangle = \langle \Delta I^2 \rangle / I_0^2$. According to Domb [44], the density fluctuations are related to the isothermal compressibility according to the following relationship:

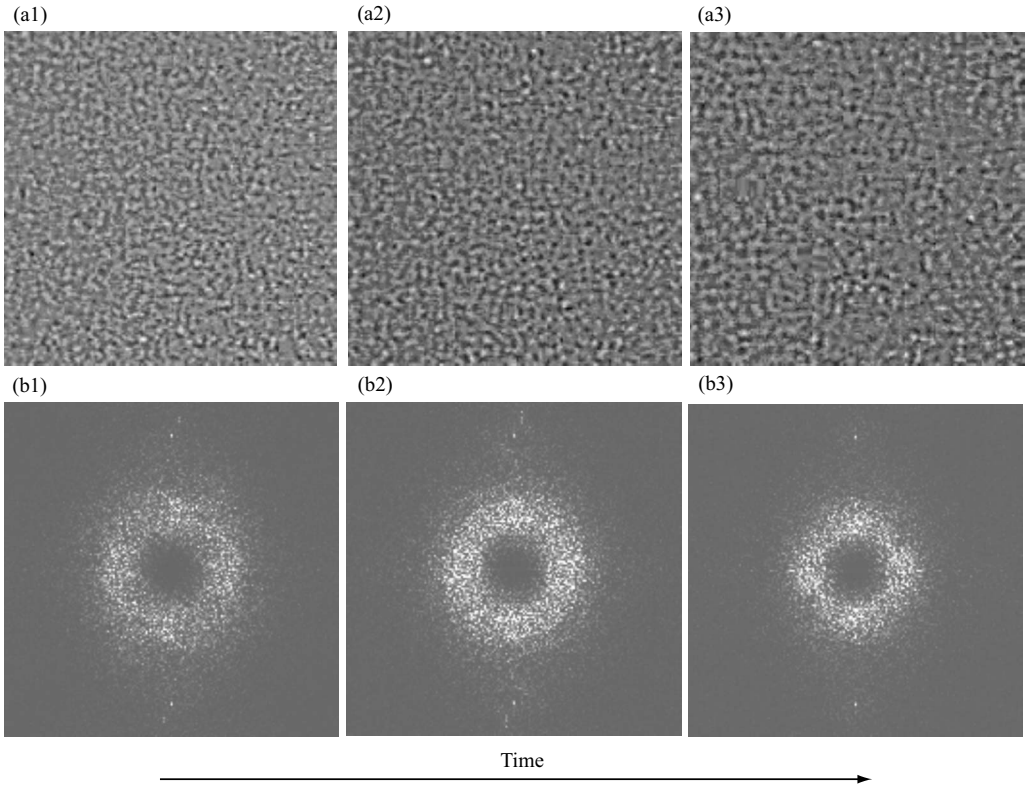


FIG. 6. Fluctuation images were obtained by subtracting the filtered image from the original image (a). The corresponding power spectra (b) show a characteristic ring corresponding to a maximum of FFT power spectrum. The ring's associated characteristic wave number is a good estimate of the characteristic length associated to the fluctuating images shown in panels (a).

$$\frac{\langle \Delta\rho^2 \rangle}{\rho_c^2} = c k_B T_c k_T / V, \tag{5}$$

where $k_B$ is Boltzmann's constant, $\rho_c$ is the critical density, $T_c$ is the critical temperature, $V$ is the volume of fluid covering one pixel (3.1 $\mu$m) in the recording image at a depth of $t_0 = 1.9$ $\mu$m, and $k_T$ is the isothermal compressibility. Near the critical point, the isothermal compressibility of a fluid is given by the power law [45]

$$k_T = k_0 \left( \frac{T - T_c}{T_c} \right)^{-\gamma}, \tag{6}$$

where $k_0 = 1.33 \times 10^{-8}$ m$^2$/N, and $\gamma = 1.19$ for $SF_6$ [7]. By substituting (6) into (5) and the result into (4), the relative temperature, $\Delta T = |T - T_c|$, can be estimated by measuring the variance of the scattered light intensity,

$$\Delta T = T - T_c = T_c \left( \frac{k_0 k_B T_c}{V \langle \delta I^2 \rangle} \right)^{1/\gamma}. \tag{7}$$

Equation (7) allows us to estimate the temperature based on measured intensity fluctuations of the scattered light. This method has the advantage of avoiding any reference to the spatial correlation of the pixels in the recorded image, which will be affected by the finite size of the physical system. However, one observation must be made: The CCD camera records gray levels corresponding to scattered light intensity and, as a result, we determine the variance of the gray levels in the recorded image and not the variance of the intensity of

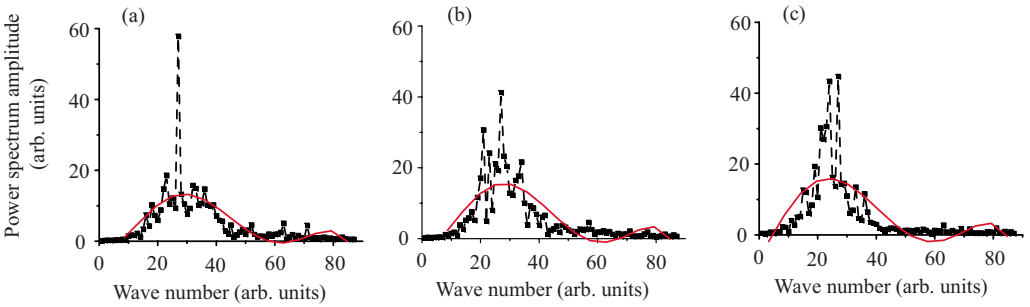


FIG. 7. (Color online) Radial average of the power spectra of fluctuation images in the "down" region [see Fig. 6(b)]. The continuous line represents the polynomial interpolation used to estimate the wave number associated with the maximum of the broad peak in the power spectrum ($k_m$).

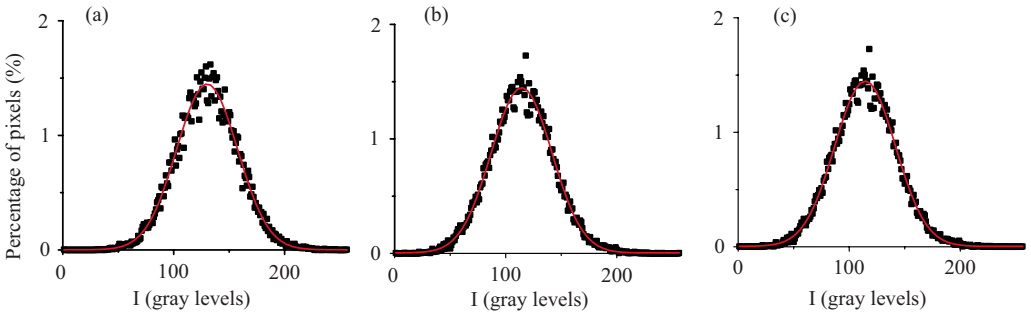


FIG. 8. (Color online) Histograms of the gray level distribution for the fluctuation images. The horizontal axis represents the gray levels from 0 to 255. The vertical axis represents the percentage of the total number of pixels corresponding to a certain gray level. The continuous line represents the Gaussian fit of the experimental histogram (filled squares). The corresponding fluctuation images are shown in Fig. 6(a).

the scattered light. According to Kammoun *et al.* [46] and Guenoun *et al.* [47], the variance of the gray levels in the background image, $\sigma_{\text{background}}$, is proportional to the gain of the camera $\Gamma \propto \sigma_{\text{background}}$. Therefore, appropriate calibration must be performed [45] in order to directly link the gray level $i=1,2,\ldots,256$ and the corresponding light intensity $I$ scattered by the fluid,

$$I \propto \frac{i^2}{\Gamma} \propto \frac{i^2}{\sigma_{\text{background}}}. \tag{8}$$

Taking into account the above observation, we developed a method for estimating the relative temperature of a fluid based on the histogram of the recorded images. According to (8), the variation of the scattered light intensity around the average value of the gray levels $\langle i \rangle$ is

$$\langle \delta I \rangle \propto \frac{\langle i \rangle \sqrt{\langle \delta i^2 \rangle}}{\sigma_{\text{background}}} \propto \frac{\langle i \rangle \sigma_i}{\sigma_{\text{background}}}, \tag{9}$$

where $\sigma_i$ is the variance of the gray levels in the image. By substituting (9) into (4), one finds that a small density fluctuation induces a change in the scattered light intensity that can be estimated using the average gray scale intensity, $\langle i \rangle$, and the variance, $\sigma_i$, of the recorded picture of the cell

$$\langle \delta \rho \rangle = b \langle i \rangle \frac{\sigma_i}{\sigma_{\text{background}}}, \tag{10}$$

where $b$ is a calibration constant. In order to determine the calibration constant $b$, we used images recorded at the beginning of the experiment at temperatures higher than the critical temperature. The estimated average gray level intensity, $\langle i_0 \rangle$, and variance, $\sigma_{i,0}$, are related to the calibration constant

$$b = \delta \rho_0 \frac{\sigma_{\text{background}}}{\langle i_0 \rangle \sigma_{i,0}}, \tag{11}$$

where $\delta \rho_0 = (\rho - \rho_c)/\rho_c = 0.0 \pm 0.02$ % at the beginning of the experiment. Finally, substituting the calibration constant (11) into (10) we determined the local density fluctuations $\delta \rho$ using the average gray levels intensity, $\langle i \rangle$, and the variance, $\sigma_i$, of the histogram of recorded images

$$\delta \rho = \delta \rho_0 \frac{\langle i \rangle \sigma_i}{\langle i_0 \rangle \sigma_{i,0}}. \tag{12}$$

After substituting (12) into (5) and the result into (7) it was possible to derive an explicit relationship for the relative temperature of the fluid,

$$\Delta T_i = T - T_c = T_c \left( \frac{k_0 k_B T_c (\langle i_0 \rangle \sigma_{i,0})^2}{V \delta \rho_0^2 (\langle i \rangle \sigma_i)^2} \right)^{1/\gamma} = \frac{30.158\ 658\ 12}{(\langle i \rangle \sigma_i)^{2/\gamma}}, \tag{13}$$

where $k_0 = 1.33 \times 10^{-8}$ m$^2$/N, $k_B = 1.38 \times 10^{-23}$ J/K is Boltzmann's constant, $T_c = 318.687$ K, and $\gamma = 1.19$ for $SF_6$ [7], $V$ is the volume corresponding to an image area of 1 pixel $= 3.1$ $\mu$m and a field depth of $t_0 = 1.9$ $\mu$m, meaning $V = 3.1$ $\mu$m $\times 3.1$ $\mu$m $\times 1.9$ $\mu$m $= 1.76 \times 10^{-17}$ $\mu$m$^3$. The depth of focus is $t_0 \approx \lambda_0/(4N_A^2)$, where the wavelength of the laser light was $\lambda_0 = 633$ nm and the numerical aperture of the optical system $N_A = 0.2$ [48]. We used 36 background frames extracted from the video recording to find the average of the gray levels intensity $\langle i_0 \rangle = 129 \pm 2$ arbitrary units with a variance $\sigma_{i,0} = 21.3 \pm 0.6$ arbitrary units. The range of average background intensity $\langle i_0 \rangle$ was between 108 and 155, and the range for the variance $\sigma_{i,0}$ of the histograms was between 14 and 29. Based on the complete set of video recordings for the "down" region, we found that the average gray level intensity was $\langle i \rangle = 114 \pm 9$ arbitrary units, the variance was $\sigma_i = 26 \pm 2$ arbitrary units, and the estimated temperature difference was $\Delta T_i = 46.74 \pm 0.03$ $\mu$K with a range from 36.19 $\mu$K to 67.32 $\mu$K. This temperature is within the temperature quench separating the "up" and "down" regions, which was 300 $\mu$K and included the critical point. Near the critical point, the correlation length also follows a power law [4]

$$\xi = \xi_0 \left( \frac{T - T_c}{T_c} \right)^{-\nu}, \tag{14}$$

where the scaling coefficient of the correlation length is $\xi_{0,\text{down}} = 0.9 \times 10^{-10}$ m, $T_c = 318.687$ K, and $\nu = 0.633$ for $SF_6$ [7]. Based on this new estimation of the temperature, $\Delta T_i$, the average value for the correlation length from (3) is $\xi_i = 2.08 \pm 0.008$ $\mu$m, which is below the pixel resolution of 3.1 $\mu$m. The index $i$ for the correlation length emphasizes that the value was derived using the estimated temperature

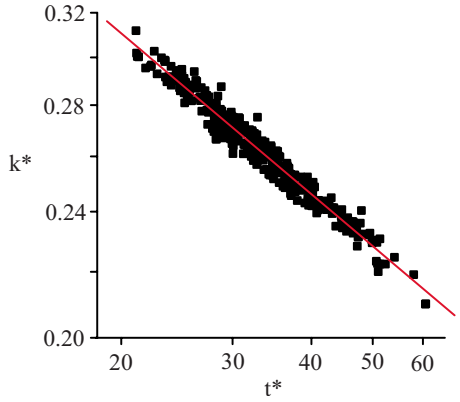


FIG. 9. (Color online) Early growth law in pure fluid ($SF_6$) when gravity effects are absent. The slowly changing wave number is an indication of slow growth of fluctuations that can be captured in a log-log plot of the scaled wave vector $k^*$ versus the reduced time $t^*$. The power law of the "down" region for 0.3 mK temperature quench shows an exponent of $-0.330 \pm 0.006$.

from the gray level histograms. Based on the above correlation length $\xi_i$, and the characteristic length $\lambda$, it is possible to compute a dimensionless quantity called the reduced wave number $k^*$, and a corresponding dimensionless reduced time ($t^*$) [49],

$$k^* = \frac{\xi}{\lambda}, \quad t^* = \frac{t}{t_\xi}, \tag{15}$$

where $t_\xi = 6\xi^3\pi\eta/(k_B T_c) = 1.71442 \times 10^{17}\xi^3$, and $\eta$ is the shear viscosity. Figure 9 shows the power law in reduced units $k^* = \xi/\lambda$ and $t^* = t/t_\xi$. The data are a reasonable fit to the universal curve with a regression coefficient of $-0.921$. The power law follows $t^{-0.330}$ growth for $SF_6$ and is similar to the power law found for the early stage of growth for shallow quenches, which is $t^{-1/3}$ [50,51].

### B. Analysis of images recorded during the 3.6 mK quench

Before the 3.6 mK quench (Fig. 2), the cell was heated to 1 K above the critical temperature $T_c$ where it equilibrated to a homogeneous state. As is seen in Fig. 10(a), the fluid separates after the temperature quench. The bright and dark spots are clusters of gas and liquid droplets with high and low density, respectively. A microscope was used to record the detailed morphology of a small area of the original image [Fig. 10(b)].

In a phase-separating fluid near the critical point it is shown that hydrodynamics plays an important role in the pattern evolution and the wetting layers are quickly formed on any solid surface [52]. In our experiment, the presence of the three thermistors inside the cell creates inhomogeneities of the density in the cell (dark spots around thermistors) caused by the wetting effects which are known to be very strong near the critical point (Fig. 10).

#### 1. Macroscopic view of phase separation for $SF_6$

Following the same procedure of image enhancement as for images corresponding to 0.3 mK quench, the power spectra of enhanced full view images [Fig. 11(a)] were determined. The enhancement of the phase-separation image resulted not only in a clearer FFT "ring," but also the horizontal and vertical lines related to the background noise were removed. For digital image processing purpose, the image obtained by subtracting the filtered image from the original image was called the phase-separating image [Fig. 11(a)]. In order to extract quantitative information from the phase-separating images, we computed their power spectra [Fig. 11(b)] [53]. The ring is broader at the beginning of the sequence and becomes narrower as we approach the end of the sequence. This means that the corresponding wave numbers are larger at first and decrease toward the end of the temperature quench [39]. Since the wave number is inversely proportional to the characteristic length of the clusters in the image, the characteristic length increases as the phase separation progresses.

For each frame in the full view of the phase-separation region, we extracted a typical size of the fluctuating domain, called the characteristic length ($\lambda$) related to the wave number ($k$) through Eqs. (2) and (3). As the experiment progresses, the estimated maximum of the radial average of

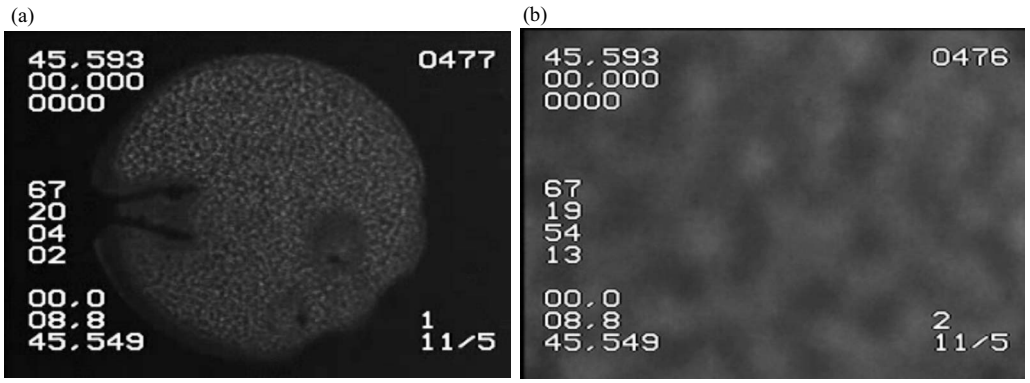


FIG. 10. Phase separation. Full (a) and microscopic (b) views of the sample cell after a 3.6 mK temperature quench. The presence of the three thermistors inside the cell creates inhomogeneities of the density in the cell (dark spots around thermistors) caused by the wetting effects which are known to be very strong near the critical point. The fluid separation in gas and liquid can be observed as domains of different brightness. The bright and dark spots of the interconnected domain are the basis of the quantitative analysis that we develop hereafter.

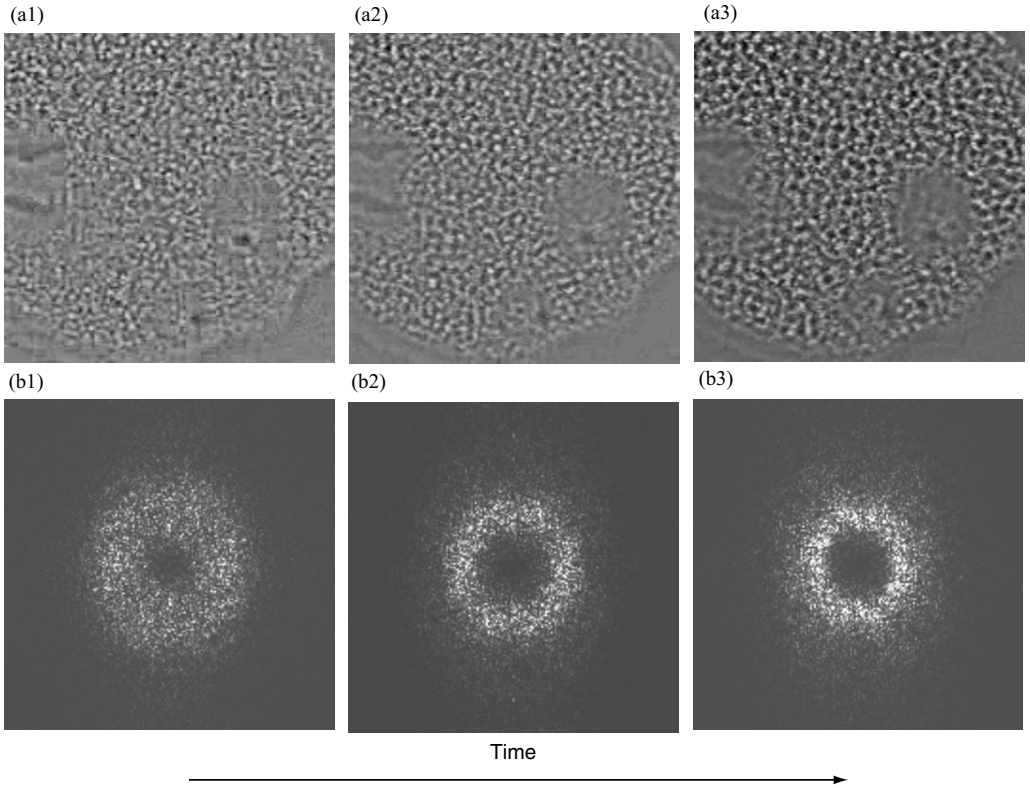


FIG. 11. Phase-separating images obtained by subtracting the filtered image from the original image for the full view case (a). Power spectra corresponding to full view phase-separating images (b). The thickness of the ring decreases as the time increases, and the wave number decreases as we move toward the end of the sequence.

the power spectrum ($k_m$) gets smaller. Based on the estimation of the wave number associated with the broad peak in the power spectrum the reduced wave number and reduced time were calculated and a growth law for the early stage of the phase separation was found (Fig. 12). The universal law indicates a $t^{-0.348}$ growth specific for the early stage.

### 2. *Microscopic view of phase separation for* $SF_6$

In the $192 \times 192$ pixels microscopic images, the density varies from high (dark clusters) to low (bright clusters) as seen in Fig. 10(b). In order to avoid including the automatically marked numbers on each frame, in our analysis we cropped all frames to a square image with the maximum possible area. As a representative example, both the power spectrum for the original image and the phase-separating microscopic image are shown in Fig. 13(a), respectively, Fig. 13(b). A comparison of the two power spectra shows bright horizontal and vertical lines that indicated a strong noise presence in the original image [Fig. 13(a)]. Following the procedure highlighted in the preceding section, we also investigated the existence of a power law between the reduced wave number $k^*$ and the reduced time $t^*$ (Fig. 14).

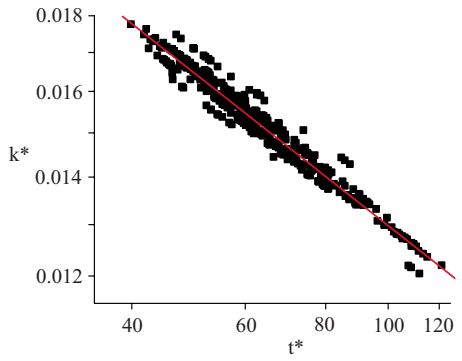


FIG. 12. (Color online) Scaling law for full view images in reduced units $k^*$ versus $t^*$. The data fit reasonably well to the early-stage growth curve. The continuous line is a linear fit to the experimental data with a slope of $-0.348 \pm 0.007$ and linear correlation $R=-0.933$ over 184 images.

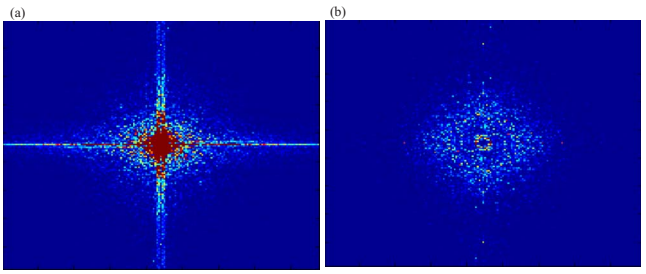


FIG. 13. (Color online) Power spectra of original (a) and filtered (b) images for microscopic view. The horizontal and vertical lines along the center of the power spectra (a) are evidence of the optical noise in the image. The FFT ring is well represented for the original noisy image, whereas by filtering the optical noise part of the FFT ring structure is lost.

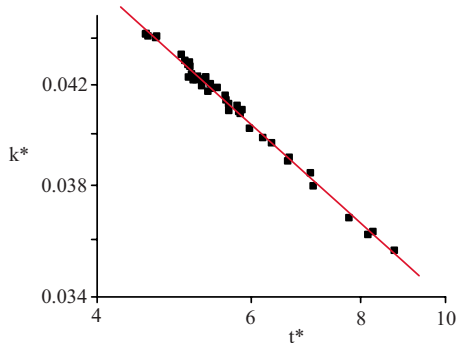


FIG. 14. (Color online) The plot of $k^*$ versus $t^*$ shows a growth law corresponding to slowly changing wave numbers (time interval 0 to 10 s). The closeness in the slope values of the two power laws for the early-stage growth demonstrates the invariance of the scale.

We plotted the reduced wave number $k^*$ versus the reduced time $t^*$ in order to extract the scaling law for the microscopic view. The exponent of the power law was $-0.341 \pm 0.01$ with a linear regression coefficient $R=-0.95$ for the region of almost constant or slowly decreasing wave numbers (Fig. 14). The fact that the exponent for the full view ($-0.348 \pm 0.007$) is close to the above exponent for the microscopic view constitutes experimental evidence of the scale invariance of the fluctuations.

#### *3. Phase separation induced by piston effect*

Above the critical temperature, the fluid under investigation is transparent and the light is transmitted [Fig. 15(a)]. After the 3.6 mK temperature quench is applied, the boundary at the cell's wall cools down. A cold boundary layer forms and its thickness increases in time. This wetting layer appears as a dark region with a well-defined shape around the cell's edge [Fig. 15(c)] and its thickness evolution can be observed in Figs. 15(d)–15(f). As a result, after lowering the temperature at the walls the thermal boundary layer contracts and the effect is an expansion in the fluids bulk [38,54,55]. This effect is amplified near the critical point because of the divergence of the thermal expansion coefficient and divergence of the isothermal compressibility. Recently, Onuki [56] presented numerical results that explained the formation of large bubble inside the cell in good agreement with our experimental results. As a consequence of the piston effect that adiabatically expands the bulk fluids, small spherical drops form as shown in Fig. 16. The fluid separates as a result of two strong concurrent effects: (1) The critical fluctuations, and (2) the piston effect. Although, the piston effect is not described in this paper in detail, we present here experimental observation supporting Onuki's computational model [56].

## V. CONCLUSIONS

The direct visualization and analysis of critical fluctuations and phase separating in pure fluids in microgravity provides invaluable information about cooperative phenomena and the role played by the thermodynamic fluctuations in determining the critical behavior. Density fluctuations appear as domains with different intensities compared to the average value of the image intensity and are detectable only near the critical point. The images analysis provides valuable information regarding the underlying statistical physics of the system. Image processing techniques, such as the radial average power spectrum, allowed us to estimate important characteristics of the fluctuations and phase-separating domains. We observed and extended the growth law in pure fluids that, when plotted in units scaled by $\xi$ and $\tau$, appears to match the growth law observed in binary liquids.

Thus there does appear to be universality to the growth law that matches the previously observed early-stage growth law. The power law for the early-stage growth shows that there is neither Brownian motion nor hydrodynamics, and gives a 1/3 growth law. One would expect a $t^1$ power law at late times with an interconnected pattern.

Two phase-separation temperature quench runs at the same density were performed on the same sample of $SF_6$ in

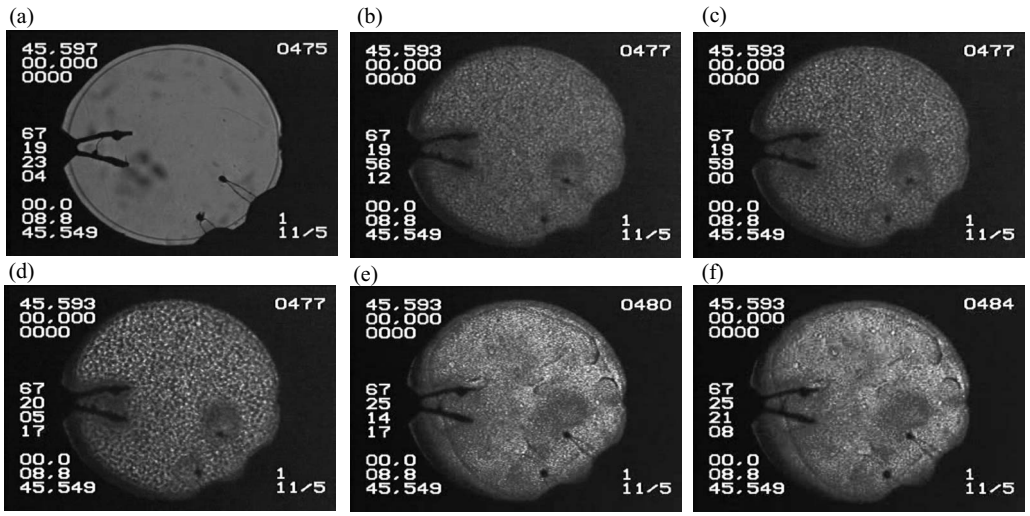


FIG. 15. The wetting layer at the edge of the cell acts as a piston adiabatically expanding the interior. The time evolution of the cell's wetting layer is recorded in frames (b), (c), (d), (e), and (f). The first image (a) was recorded above $T_c$ and is considered a reference image.

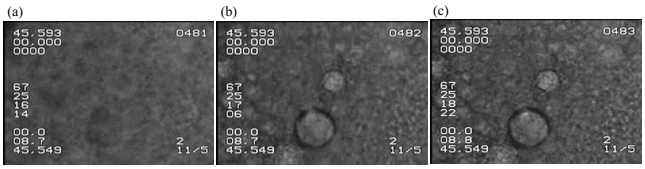


FIG. 16. The apparition of the spherical droplets in the microscopic images is caused by two concurrent effects: The critical fluctuations and the piston effect. The evolution of the droplets is observed as a shadow in the beginning (a) and after less than 1 s the droplets interface becomes darker than the bulk of the fluid (b,c).

microgravity environment. Performing these experiments on the same sample greatly increases the quality of these results as there were no significant changes in the fluid properties between runs. These results, obtained in the absence of gravity effects established a quantitative relationship between the morphology and the "universal" evolution law of the patterns.

## ACKNOWLEDGMENTS

This work was supported by a Research and Development grant from the College of Charleston to A.O., NASA Grant No. NNX07AL01A to R.Q. and S.A.O., and NASA Grants No. NAG3-1906 and No. NAG3-2447 to J.J.H.

[1] F. Perrot, P. Guenoun, T. Baumberger, D. Beysens, Y. Garrabos, and B. Le Neindre, Phys. Rev. Lett. **73**, 688 (1994).
[2] J. D. Gunton, M. San Miguel, and P. S. Sahni, in *Phase Transitions and Critical Phenomena*, edited by D. Domb (Academic, New York, 1983), Vol. 8, p. 267.
[3] P. Papon, P. H. E. Meijer, and J. Leblond, *The Physics of Phase Transitions* (Springer, Berlin, 2002), Vol. 1, p. 1.
[4] D. Beysens and Y. Garrabos, Physica A **281**, 361 (2000).
[5] A. E. Bailey, W. C. K. Poon, R. J. Christianson, A. B. Schofield, U. Gasser, V. Prasad, S. Manley, P. N. Segre, L. Cipelletti, W. V. Meyer, M. P. Doherty, S. Sankaran, A. L. Jankovsky, W. L. Shiley, J. P. Bowen, J. C. Eggers, C. Kurta, T. Lorik, P. N. Pusey, and D. A. Weitz, Phys. Rev. Lett. **99**, 205701 (2007).
[6] H. E. Stanley, *Introduction to Phase Transitions and Critical Phenomena* (Oxford University Press, Oxford, 1971).
[7] M. R. Moldover, J. V. Sengers, R. W. Gammon, and R. J. Hocken, Rev. Mod. Phys. **51**, 79 (1979).
[8] M. Barmatz, I. Hahn, J. A. Lipa, and R. V. Duncan, Rev. Mod. Phys. **79**, 1 (2007).
[9] H. Furukawa, Phys. Rev. A **36**, 2288 (1987).
[10] R. Wunenburger, Y. Garrabos, C. Lecoutre-Chabot, D. Beysens, and J. Hegseth, Phys. Rev. Lett. **84**, 4100 (2000).
[11] B. Zappoli, D. Bailly, Y. Garrabos, B. LeNeindre, P. Guenoun, and D. Beysens, Phys. Rev. A **41**, 2264 (1990).
[12] H. Boukari, J. N. Shaumeyer, M. E. Briggs, and R. W. Gammon, Phys. Rev. A **41**, 2260 (1990).
[13] A. Onuki, H. Hao, and R. A. Ferrell, Phys. Rev. A **41**, 2256 (1990).
[14] A. Onuki, *Phase Transition Dynamics* (Cambridge University Press, Cambridge, 2002).
[15] P. Guenoun, D. Beysens, F. Perrot, Y. Garrabos, and A. Kumar, J. Phys.: Condens. Matter **6**, A199 (1994).
[16] S. Huang, W. I. Goldburg, and A. W. Bjerkaas, Phys. Rev. Lett. **32**, 921 (1974).
[17] C. M. Knobler and N. C. Wong, J. Chem. Phys. **85**, 1972 (1981).
[18] F. S. Bates and P. Wiltzius, J. Chem. Phys. **91**, 3258 (1989).
[19] Y. Jayalakshmi, B. Khalil, and D. Beysens, Phys. Rev. Lett. **69**, 3088 (1992).
[20] H. Tanaka, T. Yokokawa, H. Abe, T. Hayashi, and T. Nishi, Phys. Rev. Lett. **65**, 3136 (1990).
[21] E. D. Siggia, Phys. Rev. A **20**, 595 (1979).
[22] F. J. Alexander, S. Chen, and D. W. Grunau, Phys. Rev. B **48**, 634 (1993).
[23] K. Kawasaki and T. Ohta, Physica A **118**, 175 (1983).
[24] K. Koga, M. Kawasaki, T. Takenaka, and H. Hashimoto, Physica A **198**, 473 (1993).
[25] S. Puri and B. Dunweg, Phys. Rev. A **45**, R6977 (1992).
[26] O. T. Valls and J. E. Farrell, Phys. Rev. E **47**, R36 (1993).
[27] S. Bastea and J. L. Lebowitz, Phys. Rev. Lett. **78**, 3499 (1997).
[28] M. Laradji, S. Toxvaerd, and O. G. Mouritsen, Phys. Rev. Lett. **77**, 2253 (1996).
[29] V. S. Nikolayev, D. Beysens, and P. Guenoun, Phys. Rev. Lett. **76**, 3144 (1996).
[30] H. Tanaka, Phys. Rev. Lett. **72**, 1702 (1994).
[31] H. Tanaka, J. Chem. Phys. **105**, 10099 (1996).
[32] V. S. Nikolayev and D. Beysens, Phys. Fluids **9**, 3227 (1997).
[33] H. Furukawa, Phys. Rev. A **31**, 1103 (1985).
[34] D. Beysens, Y. Garrabos, V. S. Nikolayev, C. Lecoutre, J. P. Delville, and J. Hegseth, Europhys. Lett. **59**, 245 (2002).
[35] J. J. Hegseth, Y. Garrabos, V. S. Nikolayev, C. Lecoutre-Chabot, R. Wunenburger, and D. Beysens, Int. J. Thermophys. **23**, 89 (2002).
[36] J. J. Hegseth, N. Rashidnia, and A. Chai, Phys. Rev. E **54**, 1640 (1996).
[37] R. Marcout, J. F. Zwilling, J. M. Laherrere, Y. Garrabos, and D. Beysens, Microgravity Q. **5**, 162 (1995).
[38] J. Hegseth, V. S. Nikolayev, D. Beysens, Y. Garrabos, and C. Chabot, *Fourth Microgravity and Transport Phenomena Conference, Cleveland, OH*, 1998, pp. 1640–1644.
[39] A. Oprisan, Ph.D. thesis, University of New Orleans, 2006.
[40] F. Perrot, D. Beysens, Y. Garrabos, T. Frohlich, P. Guenoun, M. Bonetti, and P. Bravais, Phys. Rev. E **59**, 3079 (1999).
[41] J. Oh, J. M. Ortiz de Zarate, J. V. Sengers, and G. Ahlers, Phys. Rev. E **69**, 021106 (2004).
[42] R. C. Gonzalez and R. E. Woods, *Digital Image Processing* (Prentice-Hall, Upper Saddle River, NJ, 2008).
[43] H. Tanaka and T. Nishi, Phys. Rev. Lett. **59**, 692 (1987).
[44] C. Domb, *The Critical Point: a Historical Introduction to the Modern Theory of Critical Phenomena* (Taylor and Francis,

New York, 1996).
[45] D. Beysens, J. Straub, and D. J. Turner, *Phase Transitions and Near-Critical Phenomena* (Springer, Berlin, 1987).
[46] F. Kammoun, J. P. Astruc, and D. Beysens, Rev. Sci. Instrum. **63**, 3659 (1992).
[47] P. Guenoun, R. Gastaud, F. Perrot, and D. Beysens, Phys. Rev. A **36**, 4876 (1987).
[48] J. Hegseth, D. Beysens, and Y. Garrabos, *Symposium on thermophysical properties, Boulder, CO*, 2003, pp. 22–27.
[49] D. Beysens, P. Guenoun, and F. Perrot, Phys. Rev. A **38**, 4173 (1988).
[50] Y. C. Chou and W. I. Goldburg, Phys. Rev. A **20**, 2105 (1979).
[51] M. Joshua, J. V. Maher, and W. I. Goldburg, Phys. Rev. Lett. **51**, 196 (1983).
[52] H. Tanaka, J. Phys.: Condens. Matter **13**, 4637 (2001).
[53] H. Tanaka and T. Nishi, Phys. Rev. Lett. **59**, 692 (1987).
[54] Y. Garrabos, M. Bonetti, D. Beysens, F. Perrot, T. Frohlich, P. Carles, and B. Zappoli, Phys. Rev. E **57**, 5665 (1998).
[55] Y. Garrabos, B. Le Neindre, P. Guenoun, B. Khalil, and D. Beysens, Europhys. Lett. **19**, 491 (1992).
[56] A. Onuki, Phys. Rev. E **75**, 036304 (2007).